

Impact of Vertical Wind Shear on Gravity Wave Propagation in the Land–Sea–Breeze Circulation at the Equator

YU DU

School of Atmospheric Sciences, and Guangdong Province Key Laboratory for Climate Change and Natural Disaster Studies, Sun Yat-sen University, Guangzhou, and Southern Marine Science and Engineering Guangdong Laboratory (Zhuhai), Zhuhai, China

RICHARD ROTUNNO

National Center for Atmospheric Research, Boulder, Colorado

FUQING ZHANG

Department of Meteorology and Atmospheric Science, and Center for Advanced Data Assimilation and Predictability Techniques, The Pennsylvania State University, University Park, Pennsylvania

(Manuscript received 20 March 2019, in final form 26 July 2019)

ABSTRACT


The impact of vertical wind shear on the land–sea–breeze circulation at the equator is explored using idealized 2D numerical simulations and a simple 2D linear analytical model. Both the idealized and linear analytical models indicate Doppler shifting and attenuation effects coexist under the effect of vertical wind shear for the propagation of gravity waves that characterize the land–sea–breeze circulation. Without a background wind, the idealized sea breeze has two ray paths of gravity waves that extend outward and upward from the coast. A uniform background wind causes a tilting of the two ray paths due to Doppler shifting. With vertical shear in the background wind, the downstream ray path of wave propagation can be rapidly attenuated near a certain level, whereas the upstream ray path is not attenuated and the amplitudes even increase with height. The downstream attenuation level is found to descend with increasing linear wind shear. The present analytical model establishes that the attenuation level corresponds to the critical level where the background wind is equal to the horizontal gravity wave phase speed. The upstream gravity wave ray path can propagate upward without attenuation as there is no critical level there.

1. Introduction

The land–sea breeze is a ubiquitous phenomenon that occurs in coastal zones around the world as it is driven by the diurnally varying thermal contrast between land and sea. Since the land–sea breeze can influence local winds, temperature, convective activity, fog, and pollution near the coastal area, where large numbers of people live, it is important to improve our understanding of the land–sea breeze (Miller et al. 2003). The land–sea breeze has been studied extensively using observations (Abbs and Physick 1992; Finkle et al. 1995; Gille et al. 2005), numerical simulations (Cautenet and Rosset 1989; Du and

Rotunno 2015, 2018), and theoretical studies (Haurwitz 1947; Rotunno 1983, hereafter R83; Qian et al. 2009, hereafter Q09; Jiang 2012a). The sea–land breeze has several components including the sea–breeze circulation, the sea–breeze gravity current, the sea–breeze front, Kelvin–Helmholtz billows, and a convective internal boundary layer (Miller et al. 2003).

The land–sea–breeze circulation, characterized by onshore or offshore flows near the surface and rising or sinking currents on the either side of the coast, is the part treated by linear theory, while the other phenomena mentioned above are nonlinear features (Yan and Anthes 1987). The land–sea–breeze circulation is found to effect to the flow over and away from the coast, which may be important in explaining diurnal variations of winds or rainfall and phase relations with respect to the diurnal heating far from coastlines (Du and Rotunno 2015, 2018; Short et al. 2019). In the present study, we

 Denotes content that is immediately available upon publication as open access.

Corresponding author: Yu Du, duyuy7@mail.sysu.edu.cn

only focus on the land–sea-breeze circulation, which is the part accessible to linear theory. It was found that the land–sea-breeze circulation can be affected and modulated by latitude (or the Coriolis force) (R83; Yan and Anthes 1987; Du and Rotunno 2015), background wind (Q09; Du and Rotunno 2018), and complex coastlines and/or topography (Papanastasiou et al. 2010; Jiang 2012a; Qian et al. 2012; Li and Carbone 2015). R83 established a linear theory of the sea-breeze circulation and documented that the solution is characterized by propagating inertia–gravity waves when the latitude is equatorward of 30° whereas the solution features a trapped circulation for higher latitudes. Du and Rotunno (2015), using a long-term WRF daily simulation, verified such phenomena off the east coast of China due to the latitude differences. Q09 introduced uniform background wind into the R83 theory at the equator, resulting in the tilting of the gravity wave ray paths¹ due to Doppler shifting. Du and Rotunno (2018) further extended the linear theory with constant background wind away from the equator and also found the modulation of the inertial–gravity wave pattern by winds. Therefore, gravity waves driven by the varying thermal contrast between land and sea form part of the land–sea-breeze circulation at the equator.

However, the wind is typically not uniform in the vertical and there is always some vertical wind shear. Although some studies investigate the effect of vertical wind shear on sea-breeze front (Pearson et al. 1983; Boybeyi and Raman 1992), few studies consider the impact of vertical wind shear on the land–sea-breeze circulation. Drobinski et al. (2011) investigated the linear dynamics of the sea breeze in an alongshore thermal wind shear and found the sea-breeze circulation is tilted toward the slanted isentropes related to the thermal wind. However, how shore-perpendicular vertical wind shear influences the sea-breeze circulation is still not clear. Jiang (2012b) considers the impact of shore-perpendicular vertical wind shear on sea breezes and associated inertial gravity waves in layered analytical model. He found attenuation of the waves across the interface associated with vertical variations in the background winds. In the present study, we attempt to develop a theory for the effect of shore-perpendicular linear vertical wind shear on the land–sea-breeze circulation.

Since the land–sea-breeze circulation takes the form of inertial–gravity waves equatorward of 30° , the influence

of vertical wind shear on the land–sea-breeze circulation might be similar to the influence of vertical wind shear on gravity wave propagation (Bretherton 1966; Hines and Reddy 1967; Heale and Snively 2015). Booker and Bretherton (1967) found that propagating gravity waves are greatly attenuated as they pass through a critical level where background horizontal wind equals to the horizontal gravity wave phase speed and the Richardson number is greater than $1/4$. As the waves propagate through the critical level, the wave energy is extracted from the basic flow when the Richardson number is less than $1/4$. In other situations, gravity waves can propagate horizontally in a low-level stable layer capped by a reflecting layer of low stability ($Ri < 1/4$), which also contains a critical level (Lindzen and Tung 1976; Du and Zhang 2019). Fritts (2015) noted that the gravity waves can be prevented from propagating to higher altitudes due to either a critical level or a turning level, where intrinsic frequency (the frequency in a frame of reference moving with the background wind) equals to 0 or N (N is the Brunt–Väisälä frequency), respectively. In this paper, we examine the propagation of gravity waves of the land–sea-breeze circulation under an ambient vertical wind shear and examine the possible effects of critical levels.

In the present study, we use a combination of an idealized numerical model and an analytical model to extend the knowledge of how vertical wind shear influences the gravity wave propagation in the sea-breeze circulation at the equator. In section 2, the idealized WRF simulations of the sea-breeze circulation are conducted to compare scenarios without a background wind, with a uniform background wind and with linear vertical wind shear. Section 3 introduces an analytical model that can produce similar wave-propagation features to that in the idealized numerical model of the sea-breeze circulation. The mechanisms by which the vertical wind shear effects the sea-breeze circulation are examined through the analytical solutions discussed in section 3. Finally, the results are summarized in section 4.

2. Idealized simulations of land–sea-breeze circulation

a. Configuration of idealized WRF Model

Following the configurations from Du and Rotunno (2015, 2018), a 2D ARW version of WRF (Skamarock and Klemp 2008) is used to simulate an idealized land–sea breeze at the equator. The Coriolis parameter is set to zero (at the equator). Although our objective is the study of the sea-breeze circulation of a single coast, we

¹ The term “ray path” is used precisely as it indicates the direction defined by the group velocity of the forced internal gravity waves, and “ray” is the same as “ray path.”

TABLE 1. WRF Model and physics settings used for the experiments.

WRF settings	Value			
	Control run	ConstWind run	Shear1 run	Shear2 run
Background wind (m s^{-1})	0	3	$u = \alpha z$ when $\alpha = 1 \text{ m s}^{-1} \text{ km}^{-1}$	$u = \alpha z$ when $\alpha = 2 \text{ m s}^{-1} \text{ km}^{-1}$
Coriolis parameter (10^{-4} s^{-1})			0	
Vertical diffusion for momentum ($\text{m}^2 \text{ s}^{-1}$)			0	
Horizontal diffusion for momentum and heat ($\text{m}^2 \text{ s}^{-1}$)			0	
Vertical diffusion for heat ($\text{m}^2 \text{ s}^{-1}$)			6	
Drag coefficient at the surface (—)			0	
Heat flux over land (W m^{-2})		$20 \cos \omega t$, where ω is diurnal frequency; starting time is 1300 LST		
Heat flux over ocean (W m^{-2})			0	
Moisture flux [g m (kg s)^{-1}]			0	
Horizontal grid spacing (km)			10	
Vertical levels			51	
Longwave physics			None	
Shortwave physics			None	
Surface scheme			Thermal diffusion scheme	
Surface-layer scheme			None	
Cumulus scheme			None	
Microphysics scheme			None	
Initial lapse rate of potential temperature (K km^{-1})			5	

use periodic boundary conditions to avoid the potentially artificial effects of other choices. In effect the periodic conditions imply a series of periodically repeating islands; so, in order to mitigate the effects of the periodic lateral boundary conditions, the simulation domain extends to 18 000 km in the x direction with land in the middle spanning 6000 km and ocean occupying the remaining 12 000 km on either side. This domain is large enough to mitigate the effects of the lateral boundaries. The horizontal grid spacing is 10 km, while the vertical grids contain 51 levels with the model top at 20 km where the gravity wave-absorbing layer of 10 km is used. The simulations do not use a radiation or boundary layer parameterization scheme, while the heat flux is specified as $20 \cos(\omega t)$ (W m^{-2}) at the land surface and zero over the ocean. The horizontal scale of the coastal zone (transition between land and ocean with respect to diurnal thermal forcing) is set to 50 km. A 10-km grid can resolve this thermal contrast. We tried a 5-km grid and the simulated features of land-sea breeze are similar. A free-slip (zero stress) condition is applied for winds at the surface (drag coefficient = 0). The numerical simulations start at 1300 LST when the heat flux at the surface reaches a peak and then are integrated forward to the fifth day when the diurnally periodic solution is achieved. All results shown in the present study are for the fifth day. In the control run, the background wind is set to 0 m s^{-1} , whereas a constant background wind or background winds with vertical wind shear are specified in the sensitivity experiments.

The detailed configurations and parameters are shown in Table 1.

b. No wind and constant wind cases

Figure 1 presents the distance–height cross section of vertical velocity over a diurnal cycle from the control run. Note that coast is at $x = 0$ and the land (ocean) is on the left (right) side with horizontal grid spacing of 10 km. Similar to the analytical solution from R83, the atmospheric response (land-sea-breeze circulation) is in the form of gravity waves that extend to “infinity” along ray paths extending upward and outward from the coast. It consists of leftward- and rightward-propagating modes, which are antisymmetric. The phase speed of rays is downward and outward, while the energy propagates upward and outward and is perpendicular to the direction of the phase velocity. Furthermore, from the time–distance Hovmöller diagrams of vertical velocity at 1- and 4-km heights (Figs. 2a,b), the horizontal wavelength is around 600–800 km and the horizontal phase speed is around $6\text{--}7 \text{ m s}^{-1}$, which is consistent with the theory of Q09 when horizontal scale of the coastal zone is 50 km (their Fig. 2b).

In the “ConstWind” run, a constant background wind equal to 3 m s^{-1} is introduced (Fig. 3). As expected from Q09, the ray paths over the land and ocean become asymmetric due to Doppler shifting. With positive background wind (directed from land to ocean), the ray path over the land is more steeply inclined to the

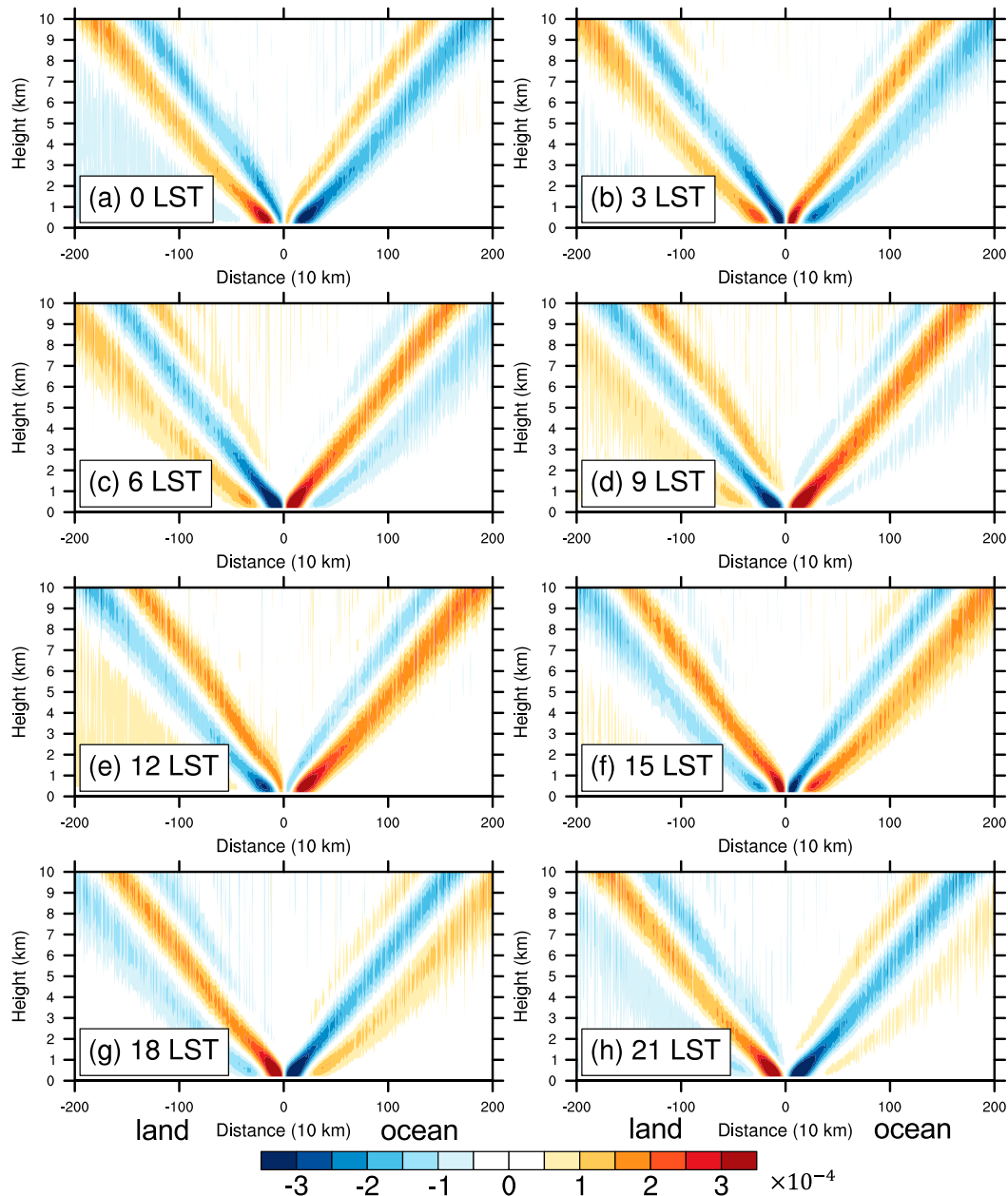


FIG. 1. Distance–height cross sections of vertical velocity (shading; m s^{-1}) over a diurnal cycle at (a) 0000, (b) 0300, (c) 0600, (d) 0900, (e) 1200, (f) 1500, (g) 1800, and (h) 2100 LST from a 2D idealized WRF Model without a background wind. Horizontal grid spacing is 10 km.

vertical, whereas the ray path over the ocean is less steeply inclined. As shown in Figs. 2c and 2d, the horizontal phase speed becomes larger (smaller) on the downstream (upstream) side compared to the control run (Figs. 2a,b). Based on the analytical solution of Q09, in addition to the two Doppler-shifted ray paths, rightward-propagating waves with negative phase tilts can be produced on the downstream side by a constant background wind; however, this effect

is not significant in the “ConstWind” run since the wind is not strong enough. With increasing background wind, the rightward-propagating waves with negative phase tilts also appear in the present idealized model (not shown).

In general, the results from the idealized WRF Model that are set up without or with a background wind are in agreement with the analytical solutions from R83 and Q09. Therefore, it is reasonable to study

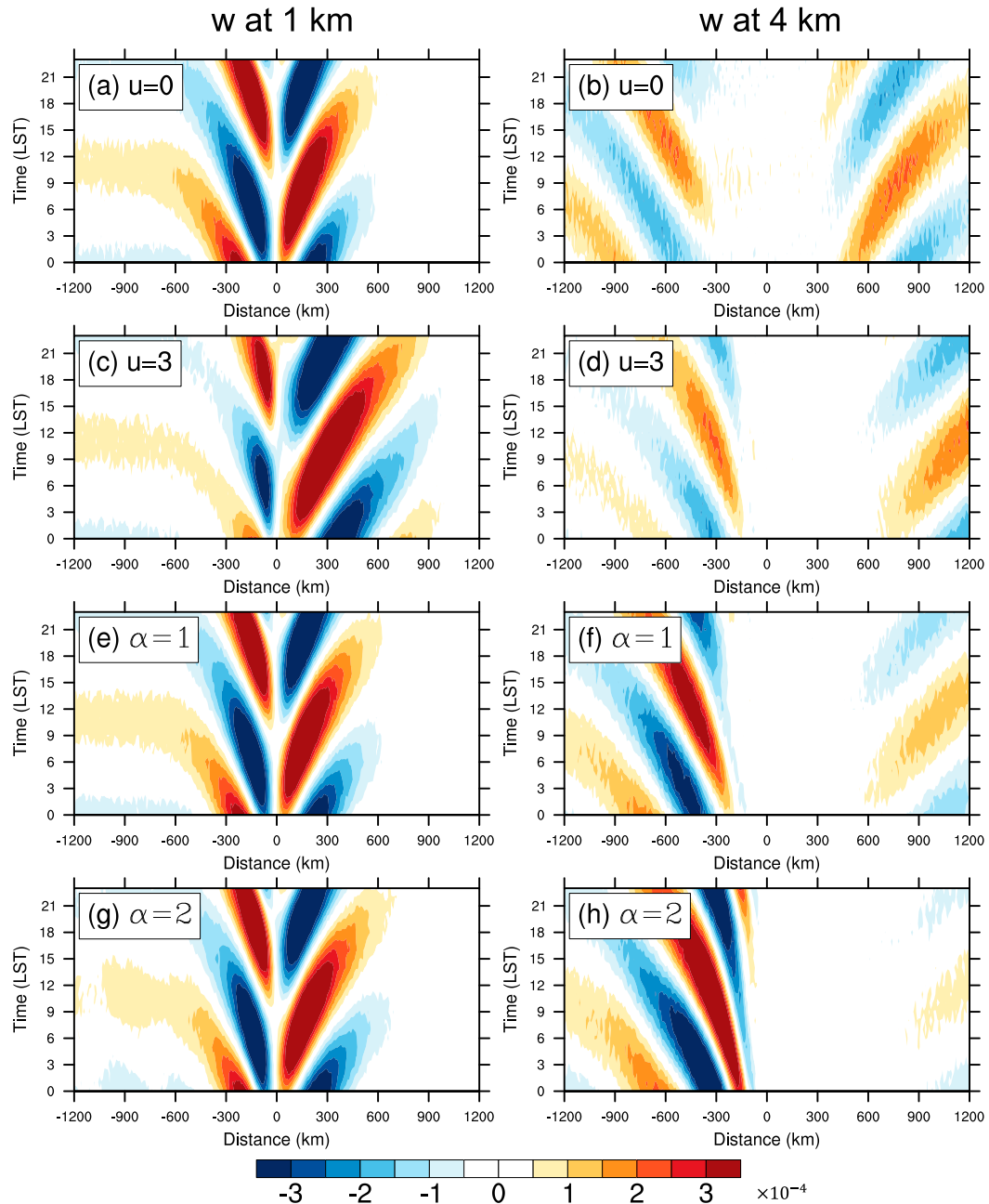


FIG. 2. Time–distance Hovmöller diagrams of vertical velocity (shading; m s^{-1}) at (a),(c),(e),(g) 1- and (b),(d),(f),(h) 4-km heights from a 2D idealized WRF Model (a),(b) without a background wind, (c),(d) with a constant wind $u = 3 \text{ m s}^{-1}$, and with a vertical wind shear α of (e),(f) 1 and (g),(h) $2 \text{ m s}^{-1} \text{ km}^{-1}$. The coast is at distance = 0.

the scenario with the vertical wind shear with the present idealized WRF Model setup, which will be discussed next.

c. Cases with vertical wind shear

With the ambient horizontal wind speed specified as $U(z) = \alpha z$ with the shear, $\alpha = 1 \text{ m s}^{-1} \text{ km}^{-1}$, the land–sea–breeze circulation structures in the “Shear1”

run over a diurnal cycle are shown in Fig. 4. Similar to the ConstWind run (Fig. 3), the ray paths of waves also tilt downstream under the background wind because of Doppler shifting. In contrast with the control run or the ConstWind run in which gravity waves extend to “infinity” along ray paths extending upward and outward from the coast, the ray paths of gravity waves over the ocean in the “Shear1” run are largely attenuated

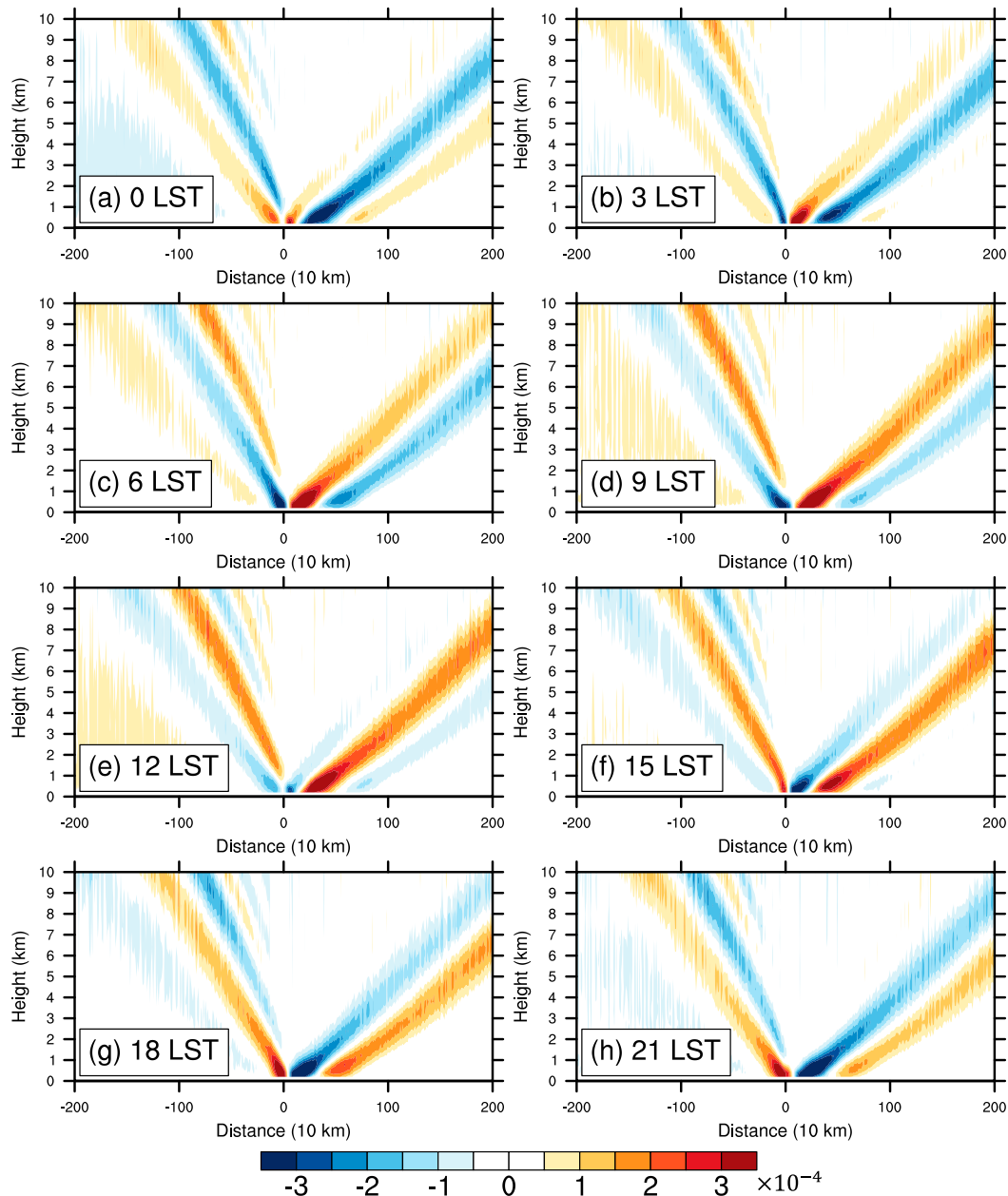


FIG. 3. As in Fig. 1, but for a constant background wind $u = 3 \text{ m s}^{-1}$.

around 6–7 km where the background wind is around $6\text{--}7 \text{ m s}^{-1}$. As indicated in the preceding section, the ground-relative horizontal phase speed is also around $6\text{--}7 \text{ m s}^{-1}$. Thus, it is likely that the 6–7-km height is a critical level. In contrast, over the land (the upstream side), the amplitude of the gravity wave increases with height and no attenuation exists.

Increasing the vertical wind shear to $\alpha = 2 \text{ m s}^{-1} \text{ km}^{-1}$ in the “Shear2” run, the level of greatest attenuation further reduces to 3–4 km (Fig. 5) where the background wind speed is around 6–8 km, which is again in

agreement with the critical-level interpretation. As the linear vertical wind shear becomes strong, the ray path over the land (ocean) is also more (less) steeply inclined to the vertical. Furthermore, the amplitude of gravity waves over the land also becomes larger. The time–distance Hovmöller diagrams of vertical velocity (Figs. 2g,h) clearly show that the magnitude of vertical velocity at 4 km largely is much smaller than that at 1 km over the ocean (downstream side), but this behavior is the opposite of that over the land (upstream side).

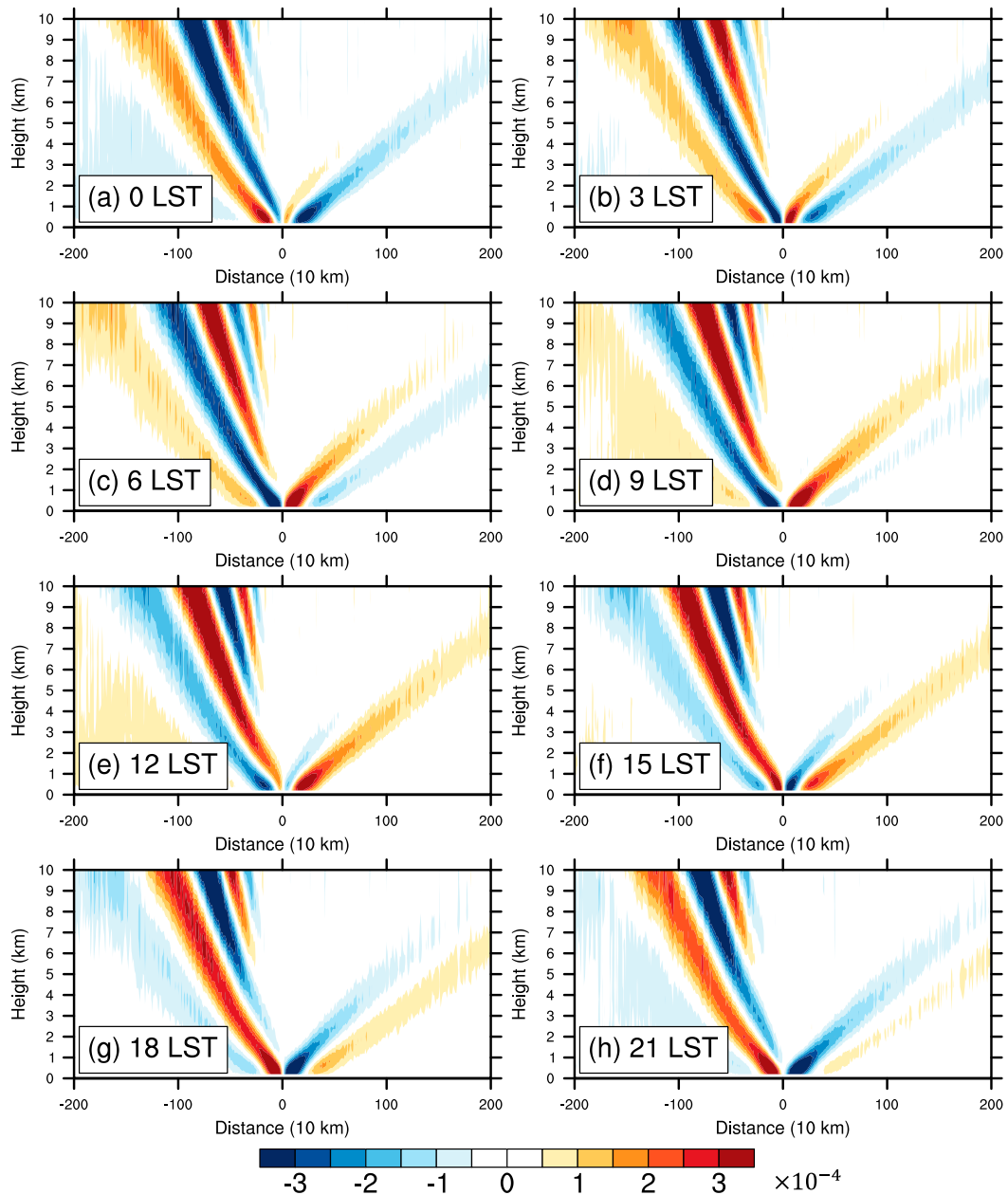


FIG. 4. As in Fig. 1, but for a vertical wind shear $\alpha = 1 \text{ m s}^{-1} \text{ km}^{-1}$.

Figure 6 shows a direct comparison among the control run, the ConstWind run, the Shear1 run, and the Shear2 run at the same time (0900 LST). Figure 6 clearly shows that tilting of the ray paths of the waves due to Doppler shifting is significant under the effect of a background wind. The attenuated or critical level descends with the increase of vertical wind shear (Figs. 6c,d). How the vertical wind shear affects the propagation of gravity waves in the land–sea–breeze circulation will be discussed in the next section with an analytical model.

3. Analytical model

a. Linear equations and analytical solutions

The traditional linear equations of land–sea–breeze model (R83; Q09; Du and Rotunno 2015, 2018) are established by specifying the diurnal heating as a forcing function in the temperature equation. When the height-dependence background wind is introduced in the traditional linear equations, the analytical solutions become far more complicated. To simplify the mathematics but retain the basic solution response to

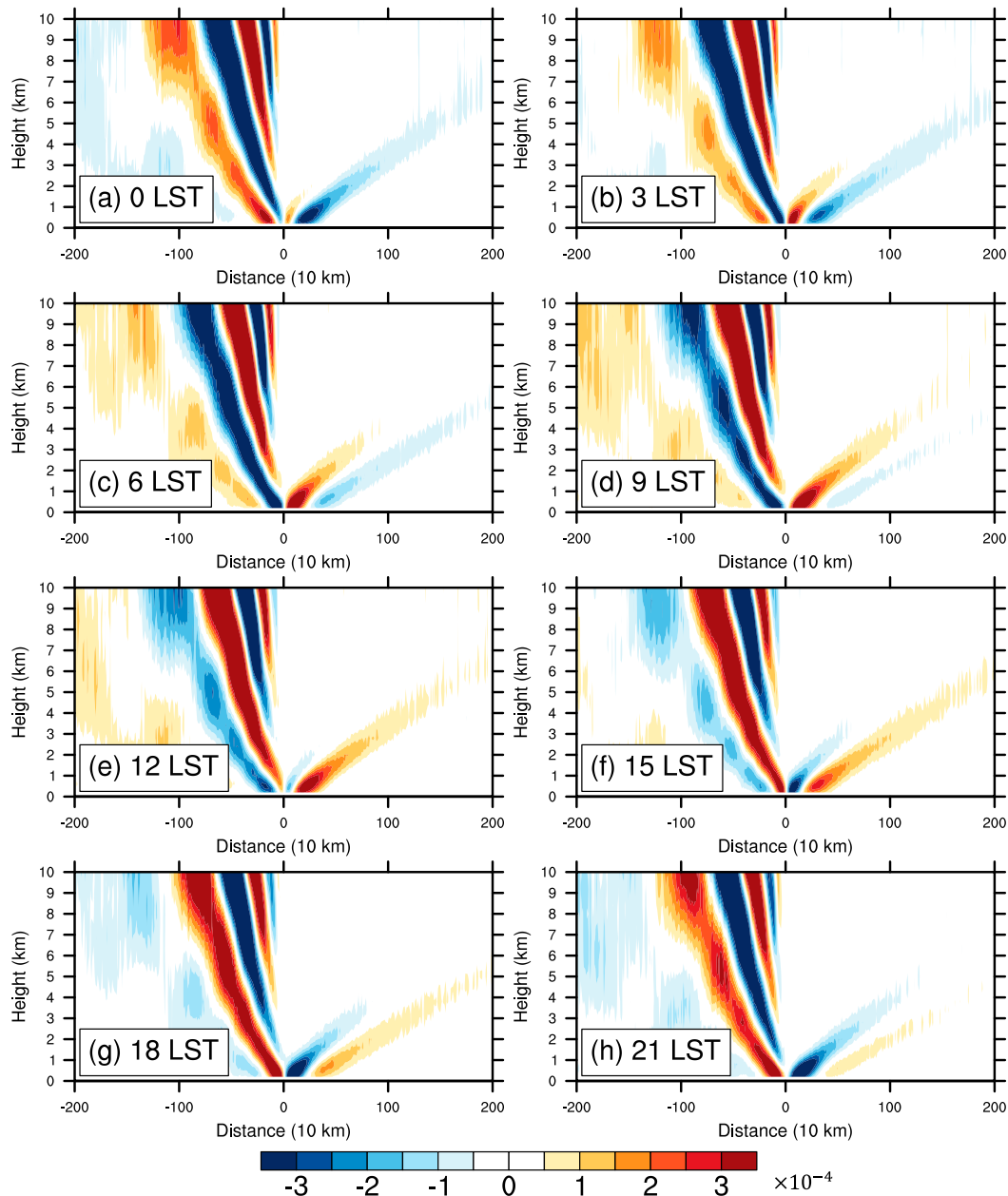


FIG. 5. As in Fig. 1, but for a vertical wind shear $\alpha = 2 \text{ m s}^{-1} \text{ km}^{-1}$.

wind shear seen in Figs. 6c and 6d, we tried a simpler model having a diurnally periodic forcing of vertical motion at the surface in the coastal zone, which can also generate gravity waves extending upward and outward along ray paths from the coast. The basic propagation features including Doppler shifting and critical-level attenuation are similar in the simpler model and the classic land–sea–breeze model.

We consider therefore the 2D linear equations of motion under the Boussinesq and hydrostatic approximations with a background vertical wind shear,

$$\left[\frac{\partial}{\partial t} + U(z) \frac{\partial}{\partial x} \right] u + w \frac{\partial U(z)}{\partial z} = -\frac{\partial \phi}{\partial x}, \quad (1)$$

$$0 = \frac{\partial \phi}{\partial z} + b, \quad (2)$$

$$\left[\frac{\partial}{\partial t} + U(z) \frac{\partial}{\partial x} \right] b + N^2 w = 0, \quad (3)$$

$$\frac{\partial u}{\partial x} + \frac{\partial w}{\partial z} = 0, \quad (4)$$

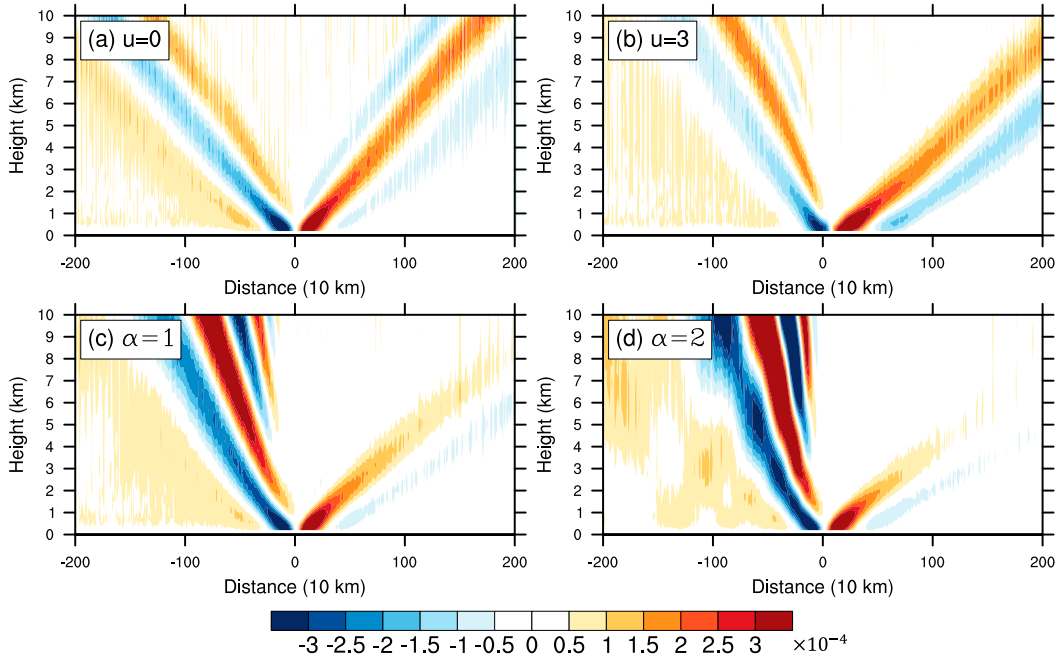


FIG. 6. Distance–height cross sections of vertical velocity (shading; m s^{-1}) at 0900 LST from a 2D idealized WRF Model (a) without a background wind, (b) with a constant $u = 3 \text{ m s}^{-1}$, and with vertical wind shear α of (c) 1 and (d) $2 \text{ m s}^{-1} \text{ km}^{-1}$.

where $U(z)$ is the background wind in the x direction; u and w are the wind components in the x and z direction, respectively; φ is the geopotential height; b is the buoyancy; and N^2 is the static stability. To emulate the effect of the usual diurnally varying heating function in Eq. (3), the lower boundary condition is specified as a diurnal forcing:

$$w(z=0) = -\frac{16\sqrt{3}}{9}w_0 \frac{a^3x}{(a^2+x^2)^2} \sin \omega t, \quad (5)$$

where w_0 is the maximum vertical velocity at the surface. The diurnal frequency $\omega = 2\pi \text{ day}^{-1}$; the function $\sin \omega t$ gives the surface vertical motion a diurnal cycle and the function, $(16\sqrt{3}/9)[a^3x/(a^2+x^2)^2]$, concentrates the diurnal forcing on either side of the coast with opposite phase; a is the horizontal scale of the diurnal forcing. The largest diurnal amplitude is at $x = \pm(\sqrt{3}/3)a$ and is equal to w_0 .

Combining Eqs. (1)–(4) into a single equation, we obtain

$$\left[\frac{\partial}{\partial t} + U(z) \frac{\partial}{\partial x} \right]^2 \frac{\partial^2 w}{\partial z^2} + N^2 \frac{\partial^2 w}{\partial x^2} = 0, \quad (6)$$

where $U(z) = \alpha z$ or $U = \text{constant}$, and z is the height.

At first, we consider the case with $U = \text{constant}$, which can be directly compared with the analytical solution of land–sea breeze from R83 ($U = 0$) and Q09 ($U \neq 0$). The Fourier transform of Eq. (6) in the x direction, using $\hat{w} = \int_{-\infty}^{\infty} w e^{-iKx} dx$, becomes

$$\left(\frac{\partial}{\partial t} + iUK \right)^2 \frac{\partial^2 \hat{w}}{\partial z^2} - K^2 N^2 \hat{w} = 0, \quad (7)$$

where K is the horizontal wavenumber. We further assume $\hat{w} = \text{Re}\{\bar{w} e^{-i(\omega t - \pi/2)}\}$, and Eq. (7) becomes

$$(-i\omega + iUK)^2 \frac{\partial^2 \bar{w}}{\partial z^2} - K^2 N^2 \bar{w} = 0. \quad (8)$$

Thus, the solution of Eq. (8) is

$$\bar{w} = A e^{i[NK/(UK-\omega)]z} + B e^{-i[NK/(UK-\omega)]z}. \quad (9)$$

According to the upward radiation condition and the lower boundary condition of $\hat{w}(z=0) = (8\sqrt{3}/9)w_0 a^2 \pi e^{-a|K|} iK$, the solution (9) becomes

$$\bar{w} = \frac{8\sqrt{3}}{9} w_0 a^2 \pi e^{-a|K|} e^{i[NK/(UK-\omega)] \text{sgn}(K)z} iK. \quad (10)$$

Applying the inverse Fourier transform, we obtain

$$w = \text{Re} \left\{ \frac{1}{2\pi} \int_{-\infty}^{\infty} \bar{w} e^{i(Kx - \omega t + \pi/2)} dK \right\}. \quad (11)$$

Thus, we obtain the solution, Eq. (11), for cases with a constant background wind in the simple model.

We now consider the case with a constant vertical wind shear, that is, $U(z) = \alpha z$. The Fourier transform in the x direction of Eq. (6), using $\hat{w} = \int_{-\infty}^{\infty} w e^{-iKx} dx$ is

$$\left[\frac{\partial}{\partial t} + iU(z)K \right]^2 \frac{\partial^2 \hat{w}}{\partial z^2} - K^2 N^2 \hat{w} = 0. \quad (12)$$

Next, applying the Laplace transform to Eq. (12), $\bar{\hat{w}} = (1/\sqrt{2\pi}) \int_0^\infty \hat{w} e^{iK\gamma t} dt$, where γ is a complex number frequency parameter, we obtain

$$\frac{\partial^2 \bar{\hat{w}}}{\partial z^2} + \frac{N^2}{(\alpha z - \gamma)^2} \bar{\hat{w}} = 0. \quad (13)$$

The corresponding lower condition boundary condition becomes

$$\bar{\hat{w}}(z=0) = \frac{1}{\sqrt{2\pi}} \left(\frac{\omega}{\omega^2 - K^2 \gamma^2} \right) \frac{8\sqrt{3}}{9} w_0 a^2 \pi e^{-a|K|} iK. \quad (14)$$

Letting $s = \alpha z - \gamma$, Eq. (13) becomes

$$s^2 \frac{\partial^2 \bar{\hat{w}}}{\partial s^2} + \frac{N^2}{\alpha^2} \bar{\hat{w}} = 0. \quad (15)$$

When we consider the situation where Richardson number $N^2/\alpha^2 > 1/4$, the solution of Eq. (15) is thus

$$\bar{\hat{w}} = A s^{1/2+i\mu} + B s^{1/2-i\mu}, \quad (16)$$

where $\mu = \sqrt{(N^2/\alpha^2) - (1/4)}$. The solution to Eq. (16) that satisfies the upward radiation condition and the lower

boundary condition (14) (but ignores the very minor reflection at the critical level; see Booker and Bretherton 1967) is

$$\bar{\hat{w}} = \left[\frac{1}{\sqrt{2\pi}} \left(\frac{\omega}{\omega^2 - K^2 \gamma^2} \right) \frac{8\sqrt{3}}{9} w_0 a^2 \pi e^{-a|K|} iK \right] \times (1 - \alpha z/\gamma)^{1/2+i\mu}. \quad (17)$$

Applying the inverse Laplace transform $\hat{w} = (K/\sqrt{2\pi}) \int_{-\infty}^\infty \bar{\hat{w}} e^{-iK\gamma t} d\gamma$, we obtain

$$\hat{w} = \frac{K}{2} \int_{-\infty}^\infty \left[\left(\frac{\omega}{\omega^2 - K^2 \gamma^2} \right) \frac{8\sqrt{3}}{9} w_0 a^2 \pi e^{-a|K|} iK \right] \times (1 - \alpha z/\gamma)^{1/2+i\mu} e^{-iK\gamma t} d\gamma, \quad (18)$$

and with $s = K\gamma$, Eq. (18) becomes

$$\hat{w} = \frac{1}{2} \int_{-\infty}^\infty \left[\left(\frac{\omega}{\omega^2 - s^2} \right) \frac{8\sqrt{3}}{9} w_0 a^2 \pi e^{-a|K|} iK \right] \times (1 - K\alpha z/s)^{1/2+i\mu} e^{-ist} ds. \quad (19)$$

Based on the residue theorem applied to a contour that is a semicircle in the lower half of the complex- s plane and deformed into the upper half to enclose the singularities at $s = \pm \omega$ (the singularity at $s = 0$ is removable), we obtain

$$\begin{aligned} \hat{w} &= 2\pi i \sum \text{Residues} = \pi i \left\{ \lim_{s \rightarrow -\omega} (s + \omega) \left[\left(\frac{\omega}{\omega^2 - s^2} \right) \frac{8\sqrt{3}}{9} w_0 a^2 \pi e^{-a|K|} iK \right] (1 - K\alpha z/s)^{1/2+i\mu} e^{-ist} \right. \\ &\quad \left. + \lim_{s \rightarrow \omega} (s - \omega) \left[\left(\frac{\omega}{\omega^2 - s^2} \right) \frac{8\sqrt{3}}{9} w_0 a^2 \pi e^{-a|K|} iK \right] (1 - K\alpha z/s)^{1/2+i\mu} e^{-ist} \right\} \\ &= \left[\frac{(1 + K\alpha z/\omega)^{1/2+i\mu} e^{i\omega t} - (1 - K\alpha z/\omega)^{1/2+i\mu} e^{-i\omega t}}{2i} \right] \frac{8\sqrt{3}}{9} w_0 a^2 \pi e^{-a|K|} iK. \end{aligned} \quad (20)$$

Applying the inverse Fourier transform $w = (1/2\pi) \int_{-\infty}^\infty \hat{w} e^{iKx} dK = \text{Re} \{ (1/\pi) \int_0^\infty \hat{w} e^{iKx} dK \}$, we obtain

$$w = \text{Re} \left\{ \frac{8\sqrt{3}}{9} w_0 a^2 \int_0^\infty \left[\frac{(1 + K\alpha z/\omega)^{1/2+i\mu} e^{i\omega t} - (1 - K\alpha z/\omega)^{1/2+i\mu} e^{-i\omega t}}{2i} \right] e^{-a|K|} e^{iKx} iK dK \right\}. \quad (21)$$

Thus, we obtain the solution (21) for cases with linear vertical wind shear as the basis for a simple analytical model.

For completeness, we give here the nondimensional form of Eqs. (10) and (11),

$$\tilde{w} = \text{Re} \left\{ \frac{4\sqrt{3}}{9} \tilde{w}_0 \int_{-\infty}^\infty e^{-|\tilde{K}|} e^{i[\tilde{K}/(\tilde{K} - \tilde{\omega})](Na/U) \text{sgn}(\tilde{K}) \tilde{z}} e^{i(\tilde{K}\tilde{x} - \tilde{\omega}\tilde{t} + \pi/2)} i\tilde{K} d\tilde{K} \right\}, \quad (22)$$

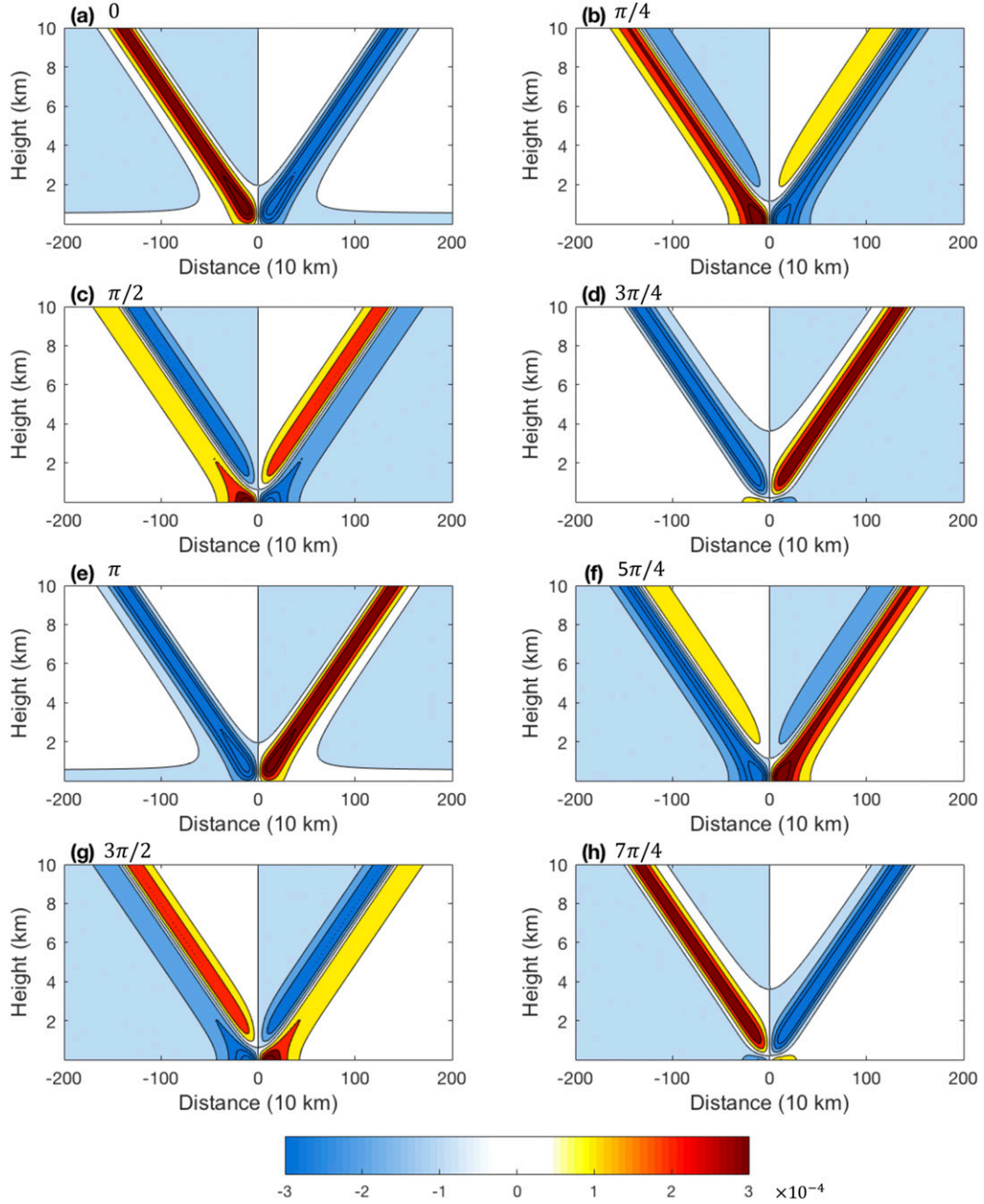


FIG. 7. Distance–height cross sections of vertical velocity (shading; m s^{-1}) over a diurnal cycle at (a) 0, (b) $\pi/4$, (c) $\pi/2$, (d) $3\pi/4$, (e) π , (f) $5\pi/4$, (g) $3\pi/2$, and (h) $7\pi/4$ phase time from the analytical model without a background wind.

And the nondimensional form of Eq. (21)

$$\tilde{w} = \text{Re} \left\{ \frac{8\sqrt{3}}{9} \tilde{w}_0 \int_0^\infty \left[\frac{(1 + \tilde{K}\tilde{z}/\tilde{\omega})^{1/2+i\mu} e^{i\tilde{\omega}\tilde{t}} - (1 - \tilde{K}\tilde{z}/\tilde{\omega})^{1/2+i\mu} e^{-i\tilde{\omega}\tilde{t}}}{2i} \right] e^{-|\tilde{K}|} e^{i\tilde{K}\tilde{x}} i\tilde{K} d\tilde{K} \right\}, \quad (23)$$

where, $\tilde{w} = w/U$, $\tilde{w}_0 = w_0/U$, $\tilde{K} = Ka$, $\tilde{x} = X/a$, $\tilde{z} = z/a$, $\tilde{\omega} = \omega a/U$, and $\tilde{t} = tU/a$, where U is the specified ambient wind speed in the first case and $U = \alpha a$ in the second case.

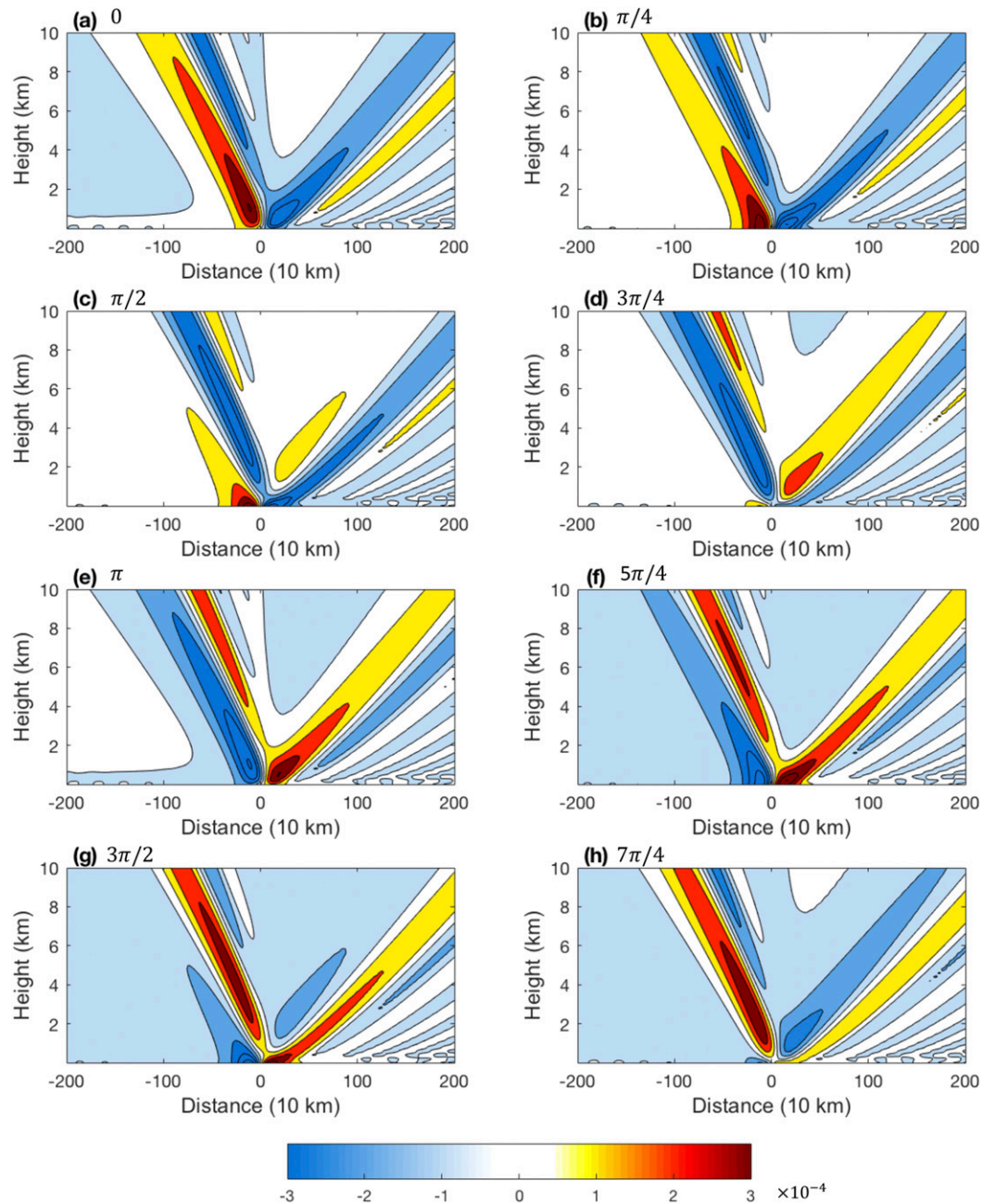


FIG. 8. As in Fig. 7, but for a constant wind $u = 3 \text{ m s}^{-1}$.

b. Evaluation of the simple analytical model

In this study, the integrations in the analytical solutions of Eqs. (11) and (21) are calculated numerically by MATLAB. To match the wave amplitude in the WRF idealized model, we set $w_0 = 5 \times 10^{-4} \text{ m s}^{-1}$ in the analytical model. Other parameters are set as $N = 0.01 \text{ s}^{-1}$ and $a = 200 \text{ km}$ in Eq. (11) or Eq. (21). These parameters are chosen based on the settings from the idealized WRF Model. We note that the form of the

diurnal forcing is not exactly same between the analytical model and the idealized WRF Model. To compare the two of them precisely, we choose the maximum of vertical motion w_0 at $z = 0$ in the analytical model to be close to the vertical velocity in the idealized WRF Model at around $z = 200 \text{ m}$. In the idealized WRF Model, the maximum of vertical motion near the surface is located at around $\pm 100 \text{ km}$. For comparison, we set $a = 200 \text{ km}$, so that $x = \pm(\sqrt{3}/3)a \sim 100 \text{ km}$.

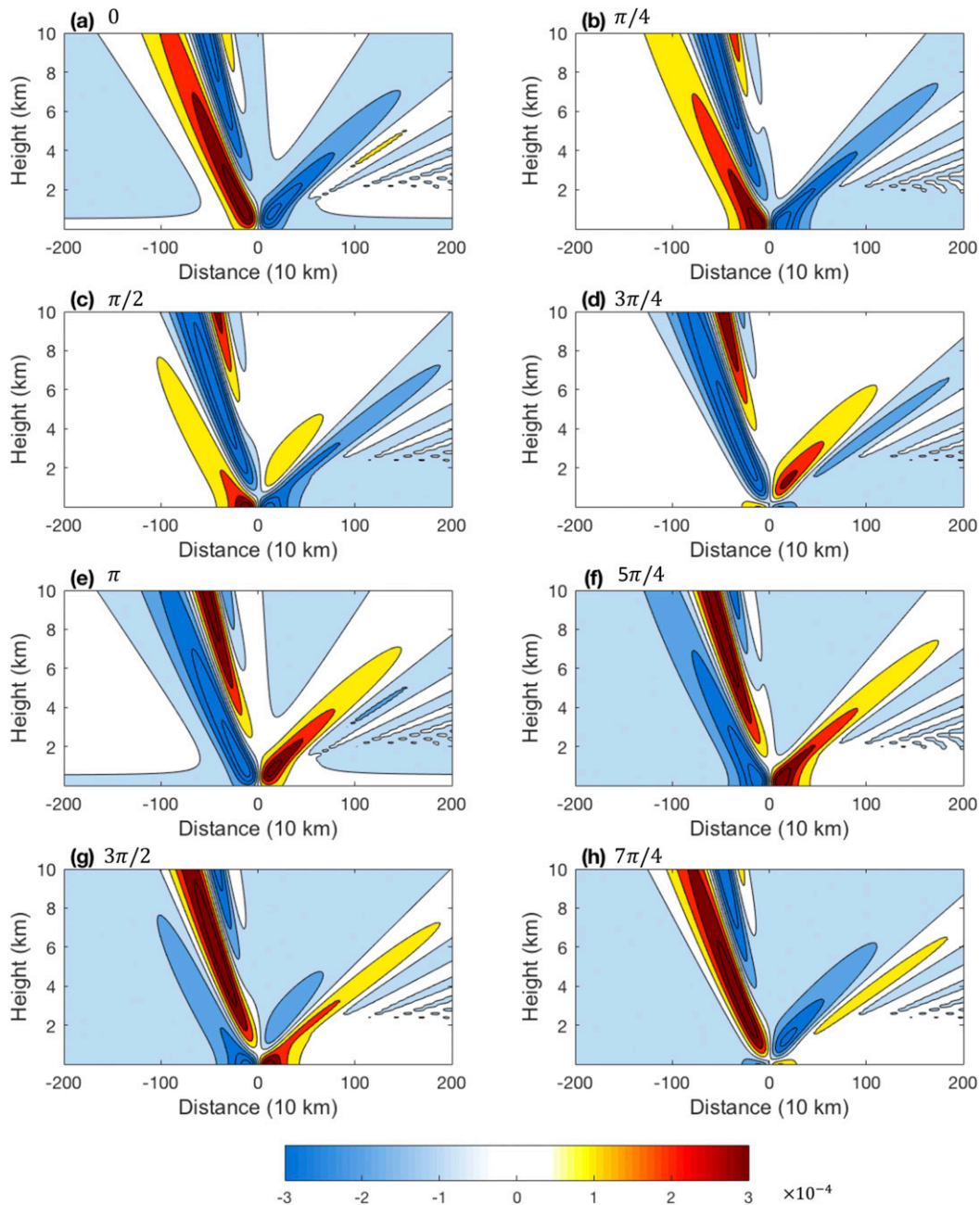


FIG. 9. As in Fig. 7, but for a linear vertical wind shear $\alpha = 1 \text{ m s}^{-1} \text{ km}^{-1}$.

When the background wind is zero ($U = 0$), we obtain the diurnal cycle of the vertical velocity in the x - z plane (Fig. 7) from Eq. (11). As shown in Fig. 7, two ray paths of gravity waves extending upward and outward from $x = 0$ (coast) are antisymmetric in phase between land and ocean. The direction of the phase velocity (downward and outward) is perpendicular to that of the group velocity (or energy propagation, upward and outward). Such a wave pattern is generally similar to results from both the analytical solution of land-sea breeze from R83

or Q09 (their Fig. 1) and the WRF idealized model in the present study.

We further verify the present analytical model with a constant background wind ($U = 3 \text{ m s}^{-1}$; Fig. 8). Similar to the results from Q09 and the WRF idealized model (Fig. 3), Doppler shifting and associated wave dispersion occur under a constant background wind. The extent of the Doppler shifting is determined by the background wind speed. With increasing background wind speed, the ray path tilting becomes greater (not shown).

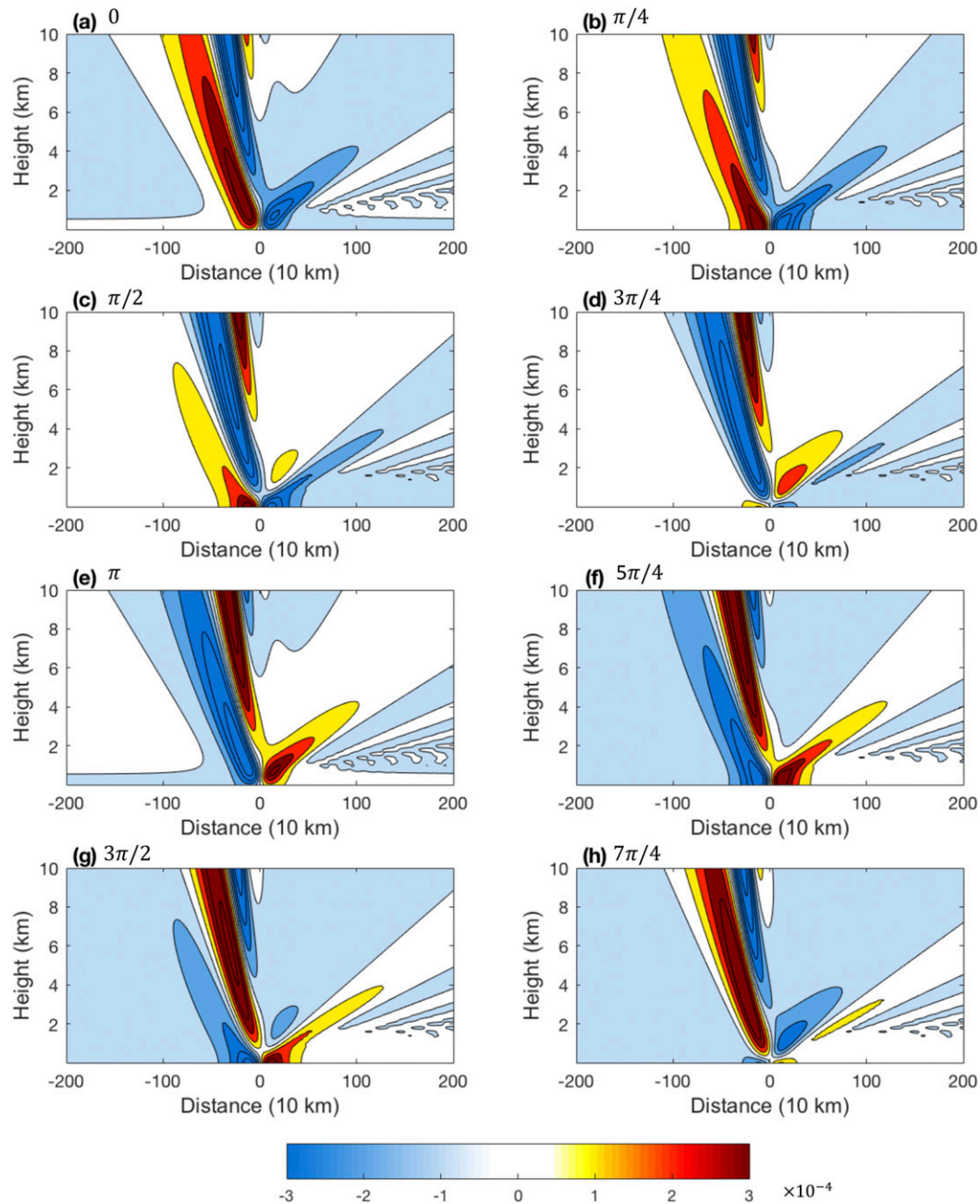


FIG. 10. As in Fig. 7, but for a linear vertical wind shear $\alpha = 2 \text{ m s}^{-1} \text{ km}^{-1}$.

Some additional waves with negative tilts over the ocean are found with larger U (not shown), which is consistent with the third branch in the solution of Q09. Therefore, with the simple numerical model setup, it is feasible to explore the impact of background flows on wave propagation.

c. Gravity wave propagation with vertical wind shear

Based on Eq. (21), we can obtain similar cross sections of vertical velocity with linear vertical wind shear

$[U(z) = \alpha z]$. First, we set very small shear α , the solution becomes quite similar to the case of $U = 0$ from Eq. (11) (not shown). When the shear is set as $\alpha = 1 \text{ m s}^{-1} \text{ km}^{-1}$, the diurnal cycle of cross section of vertical velocity is shown in Fig. 9. Similar to results from the WRF idealized simulation (Fig. 4), in addition to the tilting of rays due to Doppler shifting, the ray path over the ocean (right or downstream side) is also attenuated mostly around 6–7 km, while there is no obvious attenuation

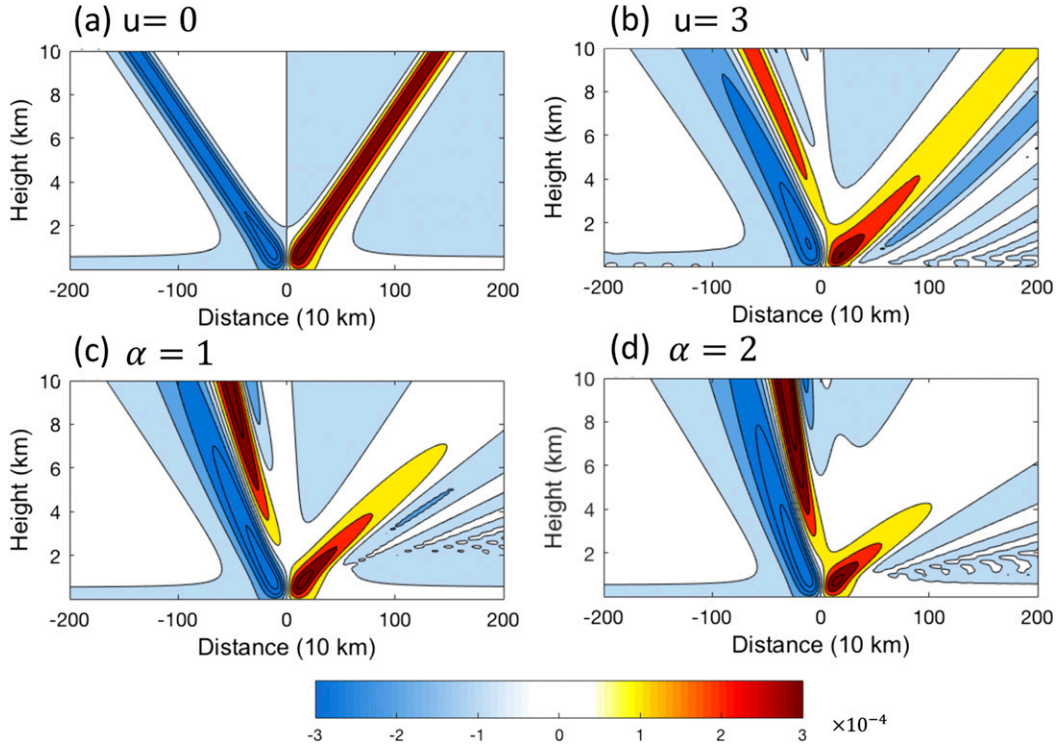


FIG. 11. Distance–height cross sections of vertical velocity (shading; m s^{-1}) at π from the analytical model (a) without a background wind, (b) with a constant background wind, and with vertical wind shear α of (c) 1 and (d) $2 \text{ m s}^{-1} \text{ km}^{-1}$.

over the land (left or upstream side). Furthermore, when the shear is set to the larger value $\alpha = 2 \text{ m s}^{-1} \text{ km}^{-1}$, the attenuation over the ocean occurs lower at around 3–4-km height (Fig. 10), which is also consistent with the results from the WRF idealized simulations (Figs. 4 and 5).

Figure 11 shows the direct comparison of wave propagations among the cases without background wind, with a constant background wind, and with vertical wind shear. This figure clearly shows that the background wind can affect the ray path tilting due to Doppler shifting, and the vertical wind shear leads to an attenuation level aloft on downstream side. Those basic features are all consistent with the 2D WRF idealized model of land–sea breeze. Since the Doppler shifting effect has already been analyzed and discussed in Q09, we will mainly focus on the mechanism of attenuation effect in the next subsection.

Similar to Fig. 2, the time–distance Hovmöller diagrams of vertical velocity at 1- and 4-km heights from the analytical model are shown in Fig. 12. The basic features including the propagation speed and amplitude under the effect of the Doppler effect and attenuation are all consistent with results from the 2D WRF idealized model.

d. Effects of vertical wind shear

In this section, through the analysis of analytical solutions from Eq. (21), the effects of vertical wind shear

on the gravity wave propagation will be explored. The solution can be divided into two terms as

$$w_1 = \text{Re} \left\{ \frac{8\sqrt{3}}{9} w_0 a^2 \int_0^\infty \left[\frac{\left(1 + \frac{K\alpha z}{\omega}\right)^{1/2+i\mu}}{2i} e^{i\omega t} \right] \times e^{-a|K|} e^{iKx} iK dK \right\} \quad (24)$$

and

$$w_2 = \text{Re} \left\{ \frac{8\sqrt{3}}{9} w_0 a^2 \int_0^\infty \left[\frac{-\left(1 - \frac{K\alpha z}{\omega}\right)^{1/2+i\mu}}{2i} e^{-i\omega t} \right] \times e^{-a|K|} e^{iKx} iK dK \right\}. \quad (25)$$

As shown in Fig. 13, the first term (w_1) represents the left ray path of gravity waves whereas the second term (w_2) represents the right ray path. In Eqs. (24) and (25),

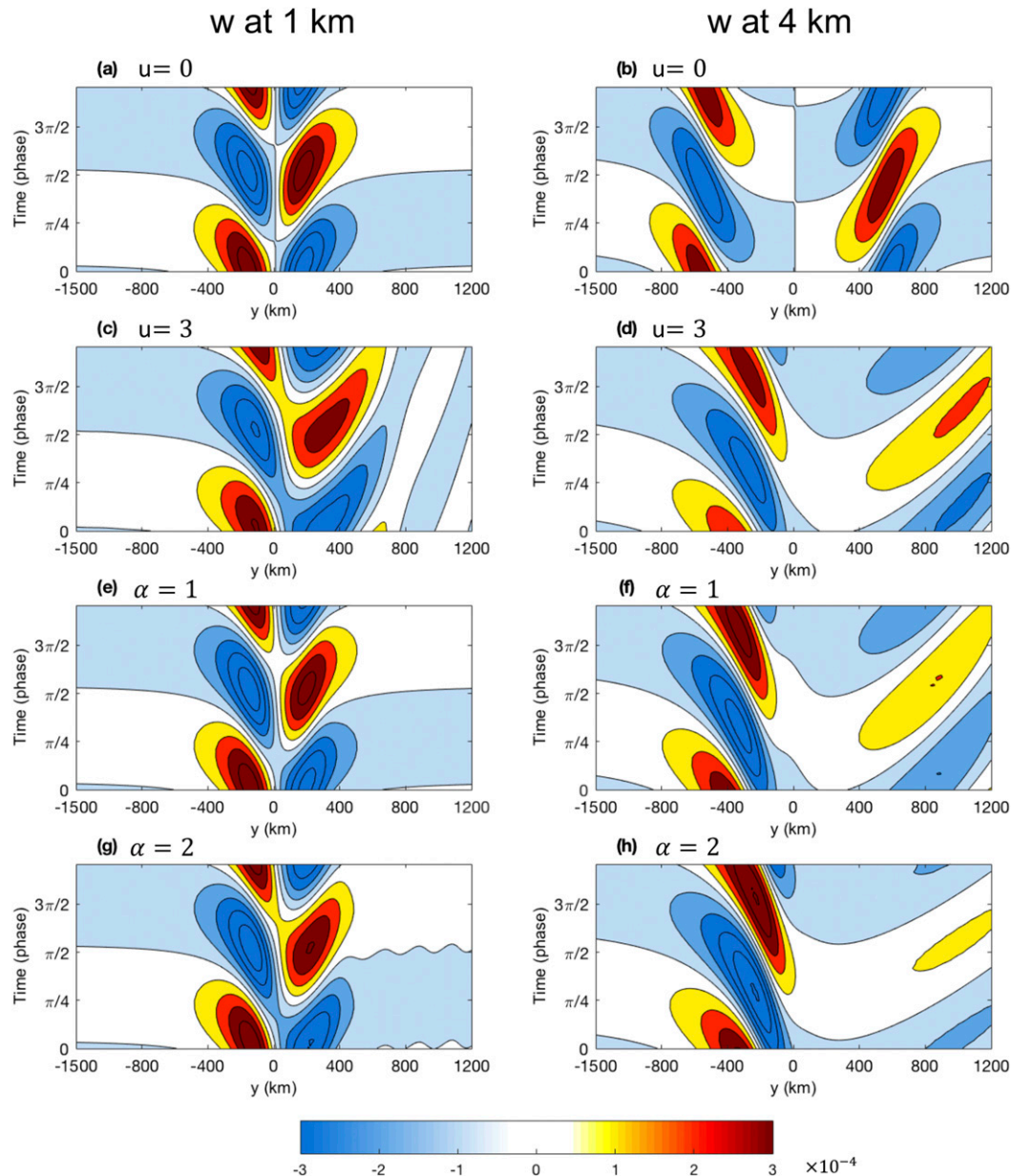


FIG. 12. Time–distance Hovmöller diagrams of vertical velocity (shading; m s^{-1}) at (a),(c),(e),(g) 1- and (b),(d),(f),(h) 4-km heights from the analytical model (a),(b) without a background wind, (c),(d) with a constant wind $u = 3 \text{ m s}^{-1}$, and with vertical wind shear α of (e),(f) 1 and (g),(h) $2 \text{ m s}^{-1} \text{ km}^{-1}$. The coast is at distance = 0.

$e^{\pm i\omega t}$ determines the leftward or rightward propagation of gravity waves. The major difference between left-side and right-side terms is the factor $(1 \pm K\alpha z/\omega)^{1/2+i\mu} = \{1 \pm [\alpha z/(c + ic_i)]\}^{1/2+i\mu}$ in Eqs. (24) and (25) where the small imaginary phase speed, c_i allows the choice of the proper branch in going from below to above the critical layer, but can be made arbitrarily small. With regard to the left-side term, the real part of $\{1 + [\alpha z/(c + ic_i)]\}$ is always positive. However, for the right-side branch, the real part of $\{1 - [\alpha z/(c + ic_i)]\}$ can be negative when $z > c/\alpha$, which for

$c_i > 0$ implies that the amplitude $|\{1 - [\alpha z/(c + ic_i)]\}^{1/2+i\mu}|$ is very small when $z > c/\alpha$. Figure 14 shows the shear-height diagram of $|\{1 \pm [\alpha z/(c + ic_i)]\}^{1/2+i\mu}|$ when $\alpha = 1 \text{ m s}^{-1} \text{ km}^{-1}$ and $c = 7 \text{ m s}^{-1}$. It is found that the value $|\{1 + [\alpha z/(c + ic_i)]\}^{1/2+i\mu}|$ increases with height for the left side (Fig. 14a), while the value $|\{1 - [\alpha z/(c + ic_i)]\}^{1/2+i\mu}|$ decreases with height for the right side (Fig. 14b). Therefore, the amplitude of gravity waves for the left-side term increases with height, while the amplitude of gravity waves for the right-side term decreases with height (Figs. 9

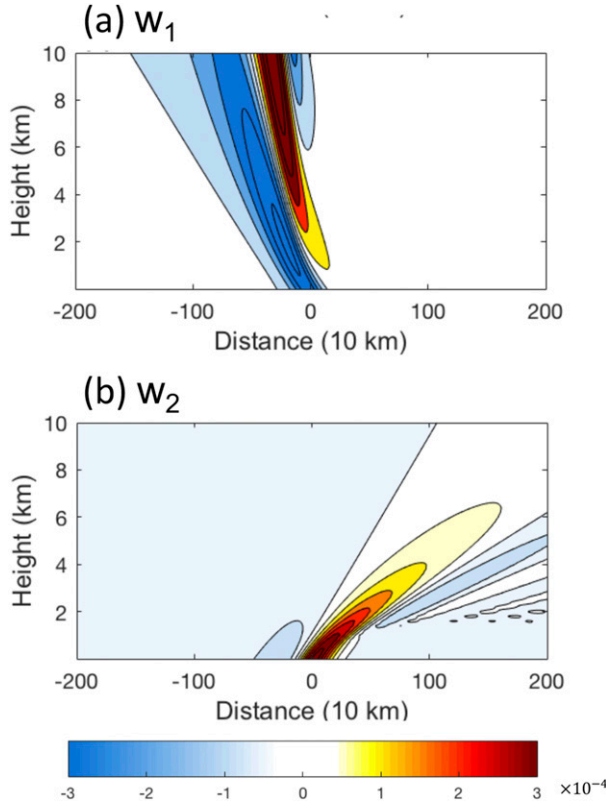


FIG. 13. Distance–height cross sections of vertical velocity (shading; m s^{-1}) at π from (a) w_1 and (b) w_2 of the analytical model with vertical wind shear $\alpha = 1 \text{ m s}^{-1} \text{ km}^{-1}$.

and 10). Furthermore, the height of largest attenuation descends with increasing α for the right-side term. For instance, the greatest gradients are located at around 6- and 3-km heights when α is equal to 1 and $2 \text{ m s}^{-1} \text{ km}^{-1}$ indicated by white triangles in Fig. 14b. The location of greatest gradients corresponds to $1 - \alpha z/c = 0$ or $z = c/\alpha$, which is related to the critical level when the background wind [$U(z) = \alpha z$] is equal to the phase velocity of gravity waves (c). On the other hand, there is no critical level for the left side because $1 + \alpha z/c > 0$, which explains why the critical level (attenuation level) only occurs on the downstream side and decreases with vertical wind shear.

4. Summary

Previous studies of the land–sea breeze have documented that the latitude, background wind, and terrain are important factors for the land–sea-breeze circulation. In terms of the background wind, uniform/constant shore-perpendicular background wind has been already introduced in the land–sea-breeze model (Q09). However, few studies consider the effect of shore-perpendicular vertical wind shear on the land–sea-breeze circulation

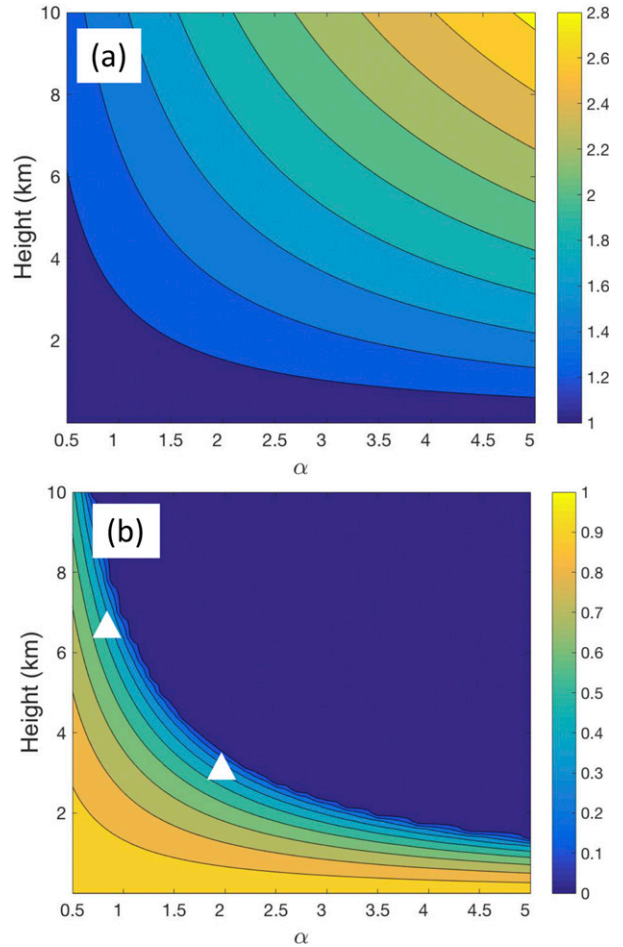


FIG. 14. Shear–height diagrams of (a) $|\{1 + [\alpha z/(c + ic_i)]\}^{1/2 + i\mu}|$ and (b) $|\{1 - [\alpha z/(c + ic_i)]\}^{1/2 + i\mu}|$. The white triangles represent attenuation levels when $\alpha = 1$ and $2 \text{ m s}^{-1} \text{ km}^{-1}$.

and related gravity waves. Therefore, in the present study, we attempt to use 2D idealized WRF Model of land–sea breeze and a simple analytical model to investigate the effects of vertical wind shear on gravity wave propagation in the land–sea-breeze circulation at the equator.

The 2D idealized WRF simulations can successfully reproduce idealized analytical land–sea-breeze circulations at the equator in which two ray paths of gravity waves from the coast that are antisymmetric as expected in R83. The ray paths will be tilted by the addition of a constant background wind due to Doppler shifting, which is also consistent with results from Q09. When linear vertical wind shear is introduced in the 2D idealized WRF simulations of land–sea breeze, in addition to Doppler shifting, the attenuation of propagation occurs on the downstream side, while the attenuation does not occur on the upstream side. Instead, the wave amplitudes increase with height on the upstream side. As vertical wind shear increases, the attenuation

level of propagation on the downstream side decreases correspondingly.

To explain such effects of vertical wind shear, we establish a simple analytical model whose basic features of gravity wave propagation are similar to those in the classic land–sea-breeze model. In the simple model, two ray paths extend upward and outward from the coast and are antisymmetric in phase. With existence of a constant background wind, the rays also tilt in the simple model. When the background wind is specified as a linear vertical shear in the analytical model, the attenuation effect of propagation on the downstream side is also found, which is similar to that found in the 2D idealized WRF Model.

By analyzing the solutions in the analytical model, we found that it is a critical level that affects the downstream propagation of gravity waves. The largest attenuation happens near the critical level. The analytical solution can be divided into the leftward and rightward rays. The wave amplitude on the left (upstream) side, which is proportional to $|1 + [\alpha z/(c + ic_i)]|^{1/2+i\mu}$, increases with height, whereas the wave amplitude on the right (downstream) side, which is proportional to $|1 - [\alpha z/(c + ic_i)]|^{1/2+i\mu}$, decreases with height and also decreases largely around $z = c/\alpha = U/\alpha$, which is the critical level.

Therefore, we find that gravity wave propagation in the land–sea-breeze circulation is largely attenuated near the critical level in addition to Doppler shifting under the effect of vertical wind shear. The present study only focuses on the effect of vertical wind shear on the land–sea-breeze circulation (treated by linear theory). The sea-breeze front or density currents in the land–sea-breeze system can also be affected by vertical wind shear, but are nonlinear features outside of scope of this study and are left to future work.

Acknowledgments. This study was supported by the National Key Research and Development Program of China (Grant 2018YFC1507402), the National Natural Science Foundation of China (Grants 41875055 and 41861164027), and the U.S. National Science Foundation (Grant AGS-1712290).

REFERENCES

- Abbs, D. J., and W. L. Physick, 1992: Sea-breeze observations and modelling: A review. *Aust. Meteor. Mag.*, **41**, 7–19.
- Booker, J. R., and F. P. Bretherton, 1967: The critical layer for internal gravity waves in a shear flow. *J. Fluid Mech.*, **27**, 513–539, <https://doi.org/10.1017/S0022112067000515>.
- Boybeyi, Z., and S. Raman, 1992: A three-dimensional numerical sensitivity study of mesoscale circulations induced by circular lakes. *Meteor. Atmos. Phys.*, **49**, 19–41, <https://doi.org/10.1007/BF01025399>.
- Bretherton, F. P., 1966: The propagation of groups of internal gravity waves in a shear flow. *Quart. J. Roy. Meteor. Soc.*, **92**, 466–480, <https://doi.org/10.1002/qj.49709239403>.
- Cautenet, S., and R. Rosset, 1989: Numerical simulation of sea breezes with vertical wind shear during dry season at Cape of Three Points, West Africa. *Mon. Wea. Rev.*, **117**, 329–339, [https://doi.org/10.1175/1520-0493\(1989\)117<0329:NSOSBW>2.0.CO;2](https://doi.org/10.1175/1520-0493(1989)117<0329:NSOSBW>2.0.CO;2).
- Drobinski, P., R. Rotunno, and T. Dubos, 2011: Linear theory of the sea breeze in a thermal wind. *Quart. J. Roy. Meteor. Soc.*, **137**, 1602–1609, <https://doi.org/10.1002/qj.847>.
- Du, Y., and R. Rotunno, 2015: Thermally driven diurnally periodic wind signals off the east coast of China. *J. Atmos. Sci.*, **72**, 2806–2821, <https://doi.org/10.1175/JAS-D-14-0339.1>.
- , and —, 2018: Diurnal cycle of rainfall and winds near the south coast of China. *J. Atmos. Sci.*, **75**, 2065–2082, <https://doi.org/10.1175/JAS-D-17-0397.1>.
- , and F. Zhang, 2019: Banded convective activity associated with mesoscale gravity waves over southern China. *J. Geophys. Res. Atmos.*, **124**, 1912–1930, <https://doi.org/10.1029/2018JD029523>.
- Finkele, K., J. M. Hacker, H. Kraus, and R. A. D. Byron-Scott, 1995: A complete sea-breeze circulation cell derived from aircraft observations. *Bound.-Layer Meteor.*, **73**, 299–317, <https://doi.org/10.1007/BF00711261>.
- Fritts, D. C., 2015: Gravity waves: Overview. *Encyclopedia of Atmospheric Sciences*, Elsevier, 142–152.
- Gille, S. T., S. G. Llewellyn Smith, and N. M. Statom, 2005: Global observations of the land breeze. *Geophys. Res. Lett.*, **32**, L05605, <https://doi.org/10.1029/2004GL022139>.
- Haurwitz, B., 1947: Comments on the sea-breeze circulation. *J. Meteor.*, **4**, 1–8, [https://doi.org/10.1175/1520-0469\(1947\)004<0001:COTSBC>2.0.CO;2](https://doi.org/10.1175/1520-0469(1947)004<0001:COTSBC>2.0.CO;2).
- Heale, C. J., and J. B. Snively, 2015: Gravity wave propagation through a vertically and horizontally inhomogeneous background wind. *J. Geophys. Res. Atmos.*, **120**, 5931–5950, <https://doi.org/10.1002/2015JD023505>.
- Hines, C. O., and C. A. Reddy, 1967: On the propagation of atmospheric gravity waves through regions of wind shear. *J. Geophys. Res.*, **72**, 1015–1034, <https://doi.org/10.1029/JZ072i003p01015>.
- Jiang, Q., 2012a: A linear theory of three-dimensional land–sea breezes. *J. Atmos. Sci.*, **69**, 1890–1909, <https://doi.org/10.1175/JAS-D-11-0137.1>.
- , 2012b: On offshore propagating diurnal waves. *J. Atmos. Sci.*, **69**, 1562–1581, <https://doi.org/10.1175/JAS-D-11-0220.1>.
- Li, Y., and R. Carbone, 2015: Offshore propagation of coastal precipitation. *J. Atmos. Sci.*, **72**, 4553–4568, <https://doi.org/10.1175/JAS-D-15-0104.1>.
- Lindzen, R. S., and K. K. Tung, 1976: Banded convective activity and ducted gravity waves. *Mon. Wea. Rev.*, **104**, 1602–1617, [https://doi.org/10.1175/1520-0493\(1976\)104<1602:BCAADG>2.0.CO;2](https://doi.org/10.1175/1520-0493(1976)104<1602:BCAADG>2.0.CO;2).
- Miller, S. T. K., B. D. Keim, R. W. Talbot, and H. Mao, 2003: Sea breeze: Structure, forecasting, and impacts. *Rev. Geophys.*, **41**, 1011, <https://doi.org/10.1029/2003RG000124>.
- Papanastasiou, D. K., D. Melas, and I. Lissaridis, 2010: Study of wind field under sea breeze conditions; an application of WRF Model. *Atmos. Res.*, **98**, 102–117, <https://doi.org/10.1016/j.atmosres.2010.06.005>.
- Pearson, R. A., G. Carbone, and G. Brusasca, 1983: The sea breeze with mean flow. *Quart. J. Roy. Meteor. Soc.*, **109**, 809–830, <https://doi.org/10.1002/qj.49710946209>.

- Qian, T., C. C. Epifanio, and F. Zhang, 2009: Linear theory calculations for sea breeze in a background wind: The equatorial case. *J. Atmos. Sci.*, **66**, 1749–1763, <https://doi.org/10.1175/2008JAS2851.1>.
- , —, and —, 2012: Topographic effects on the tropical land and sea breeze. *J. Atmos. Sci.*, **69**, 130–149, <https://doi.org/10.1175/JAS-D-11-011.1>.
- Rotunno, R., 1983: On the linear theory of the land and sea breeze. *J. Atmos. Sci.*, **40**, 1999–2009, [https://doi.org/10.1175/1520-0469\(1983\)040<1999:OTLTOT>2.0.CO;2](https://doi.org/10.1175/1520-0469(1983)040<1999:OTLTOT>2.0.CO;2).
- Short, E., C. L. Vincent, and T. P. Lane, 2019: Diurnal cycle of surface winds in the Maritime Continent observed through satellite scatterometry. *Mon. Wea. Rev.*, **147**, 2023–2044, <https://doi.org/10.1175/MWR-D-18-0433.1>.
- Skamarock, W. C., and J. B. Klemp, 2008: A time-split non-hydrostatic atmospheric model for weather research and forecasting applications. *J. Comput. Phys.*, **227**, 3465–3485, <https://doi.org/10.1016/j.jcp.2007.01.037>.
- Yan, H., and R. A. Anthes, 1987: The effect of latitude on the sea breeze. *Mon. Wea. Rev.*, **115**, 936–956, [https://doi.org/10.1175/1520-0493\(1987\)115<0936:TEOLOT>2.0.CO;2](https://doi.org/10.1175/1520-0493(1987)115<0936:TEOLOT>2.0.CO;2).